CHINESE JOURNAL OF MECHANICAL ENGINEERING
Vol. 26, No. 6, 2013

DOI: 10.3901/CJME.2013.06.1194, available online at www.springerlink.com; www.cjmenet.com; www.cjmenet.com.cn

Simulations and Experimental Investigation on Motion Stability of a Flexible Rotor-bearing System with a Transverse Crack

LI Chaofeng*, YU Hexing, ZHOU Shihua, and WEN Bangchun

School of Mechanical Engineering & Automation, Northeastern University, Shenyang, 110819, China

Received June 27, 2012; revised August 16, 2013; accepted August 26, 2013

Abstract: In the classical process for stability studies on the rotor-bearing system with crack faults, the simple discrete model is adopted for research on such problems, which neglect some needful dynamical influence factor, such as the material damping, shearing effect and gyroscopic effects, etc. Therefore, it is necessary to find a precise calculation model for simulation of the rotor-bearing system with cracks faults. In this paper, instead of the traditional simple discrete model, finite element (FE) model is adopted to investigate the motion stability of a nonlinear rotor system with crack fault. According to finite element theory, the FE model of the cracked rotor system is established firstly. It should be pointed out that the element where the crack occurs is modeled by a particular crack element and the supports at both ends are simulated by two nonlinear loads. Then, based on dimensionless and dimensionality reduction, the Newmark-β method and the shooting method are employed to study the effect of eccentricity and the depth of crack on instability speed and bifurcation feature. Furthermore, the simulation results are verified by some corresponding experiments. The simulation and experimental results show that instability speed does not change monotonically, but decreases firstly and then increases when the amount of eccentricity increases. Moreover, as the type of instability changes, the instability speed jumps concomitantly. Additionally, the presence of crack fault can disturb the oil whirl, as a result, instability speed tends to increase slightly, but it does not affect the type of instability and jumping phenomenon. This research presents an effective and convenient method which uses the finite element method (FEM) to research the motion stability of the nonlinear rotor-bearing system with cracked faults and other nonlinear force, and the proposed method can provide a theoretical reference for stability analysis and vibration control in more complex relevant rotor-bearing system.

Key words: rotor-bearing system, crack faults, finite element model, instability

1 Introduction

In the research of characteristics of rotating machinery faults, the crack faults is one of the important topics, many scholars carried out a lot of research on crack faults in different ways. GASCH[1] used hinge spring model to simulate the mechanical behavior of spindle crack, analyzed the stability of Laval rotor caused by unbalance and shaft crack. Using numerical simulation and experiments, LEE[2] show the correctness of the crack opening and closing conditions and the analytical theory of diagnoses on rotor with crack. CHAN, et al[3], studied the vibration response of the rotor system with crack and asymmetry factor between the crack and eccentric together. MENG, et al[4], analyzed stability and reliability of the cracked rotor system with Folquet theory. WAN, et al[5], investigated vibration of a cracked rotor with rotor-stator rubbing supported by sliding bearings, by using harmonic wavelet transform, they observed differences in wavelet time-frequency maps of cracked rotor with and without rubbing. ZHENG, et al[6], analyzed the stability of a rotor-bearing with a shaft crack by Chebyshev polynomial method. PATEL, et al[7], have investigated the rotor whirl characteristics of the unbalance, crack and rotor-stator rub faults by numerical and experimental method. Recently, considered the coupled bending-torsional vibration, PATEL, et al[8], investigated the nonlinear response of a rotor with rub and crack. LIU, et al[9], established differential equations of a rotor-bearing system, considering the non-linear factors such as cracks, loose and film force, the periodic motion bifurcation and stability is analyzed. With the non-linear theory developed in actual production, scholars have begun to study the nonlinear problem in complex nonlinear system. LUO, et al[10], built a two-span rotor-bearing system model with two crack faults and the oil-film force, studied the nonlinear dynamics caused by the existence of cracks and crack angle.

Seen from the above literatures, the nonlinear dynamic behavior of rotor-bearing system was mainly approached by a simple discrete model. However, an assembly rotor is a complicated system, which needs to consider more important information, such as mass/moment inertia, inner

* Corresponding author. E-mail: chfli@mail.neu.edu.cn
This project is supported by National Natural Science Foundation of China(Grant No. 51105063), and Fundamental Research Funds for the Central Universities of China(Grant Nos. N120403004, N100303001)

damping, bending and torsion vibration coupling effects, the nonlinear factors of oil film bearing, and so on. ZHENG, et al[11–12], dealt with the long-term dynamic behaviors of a high-order rotor-bearing system with multi-DOF, and proposed a new reduction method and corresponding integration technique. JING, et al[13–14], compared dynamics of the continuous model and discrete model using the fixed interface modal synthesis method.

Seen from above literatures, the FEM and reduction method is applied less for a FEM craked rotor system with nonlinear factor. In this paper, a double-disk rotor-bearing system model with crack faults is established, using the relevant calculation method to analyze the impact of the system eccentricity and crack depth on the dynamic response of the system, and a qualitative experimental verification is presented, these results provide a theoretical reference for the fault diagnosis of rotor system and vibration control.

2 Establishment of Dynamical Model

Default values of related parameters in the rotor system are as follows: inside diameter of bearing at both ends is D=44 mm, effective length L_r=20 mm; rotor shaft radius r=18 mm, length l=720 mm, outside diameter of two disk R_o=160 mm, disk thickness H=20 mm, average film thickness of bearing c=0.18 mm, unbalance of disks b=0.10 mm, The initial phase of two eccentric disk $\varphi_1=\varphi_2=0$, eccentric phase difference $\Delta\varphi=0$, absolute viscosity of lubricant μ=0.018 Pa • s.

2.1 FE model of the rotor-bearing system

The finite element model of the rotor-bearing system is shown in Fig. 1.

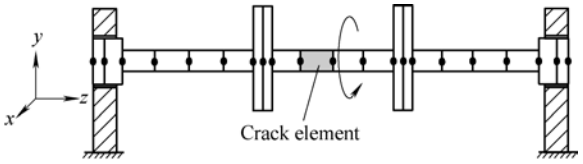

Fig. 1. FE model of the rotor-bearing system with one crack fault

The shaft is divided into 20 elements and 21 nodes according to its structural characteristics. Oil-film supporting forces are applied at 2 and 20 nodes, unbalance forces at the 8th and 12th node, respectively. The dots in the diagram indicate nodes, and each segment represents an element. The motion equation of the whole rotor system can be expressed as

$$\bar{\boldsymbol{M}}\ddot{\bar{X}}+\bar{\boldsymbol{C}}\dot{\bar{X}}+\bar{\boldsymbol{K}}\bar{X}=\bar{\boldsymbol{F}}(\bar{X},\dot{\bar{X}})+\boldsymbol{R}(t)+\boldsymbol{G}, \tag{1}$$

where $\bar{\boldsymbol{C}}=(\boldsymbol{D}+\boldsymbol{J}\bullet\omega)$, $\bar{X}=[q_1,q_2,\cdots,q_i,\cdots,q_n]^{\mathrm{T}}$ (n=21), $q_i=[x_i,y_i,\theta_{xi},\theta_{yi}]$ (i=1, 2, $\cdots$, 21). $\bar{\boldsymbol{M}}$, $\bar{\boldsymbol{K}}$ and $\bar{\boldsymbol{C}}$ are the mass, stiffnes and damping matrix; $\boldsymbol{D}$ is the material damping matrix; $\boldsymbol{J}$ is the gyro matrix; ω is the angular velocity; $\bar{\boldsymbol{F}}$ is the supporting force vector; $\boldsymbol{R}$ is the unbalanced force vector; $\boldsymbol{G}$ is the gravity vector and $\bar{\boldsymbol{X}}$ is the displacement vector.

The material damping coefficient is defined in the form of Rayleigh damping as follows:

$$\boldsymbol{D}=\alpha\bullet\boldsymbol{M}+\beta\bullet\boldsymbol{K}, \tag{2}$$

where $\alpha=2\left(\frac{\xi_2}{\omega_2}-\frac{\xi_1}{\omega_1}\right)\Big/\left(\frac{1}{\omega_2^2}-\frac{1}{\omega_1^2}\right)$,

$$\beta=2(\xi_2\omega_2-\xi_1\omega_1)/(\omega_2^2-\omega_1^2).$$

ξ_1,ξ_2 are the damping coefficient, ω_1,ω_2 are the former two order critical speed. The first three critical speeds and damping coefficients of the simple support system are shown in Table 1.

Table 1. Critical speeds and damping coefficients

Critical speed ω/(rad • s^{-1})			Material damping coefficient	
1st	2nd	3rd		
559.334	2 454.529	6 117.442	ζ_1=0.05	ζ_2=0.08

The oil-film force vector $\bar{\boldsymbol{F}}(X,\dot{X})$ in system equation is

$$\boldsymbol{F}(\bar{X},\dot{\bar{X}})=[0,\cdots,F_{xi},F_{yi},\cdots,0]^{\mathrm{T}},i=2,13,$$

$$\boldsymbol{F}_{xi}=F_x(\bar{x}_i,\bar{y}_i,\dot{\bar{x}}_i,\dot{\bar{y}}_i),\quad \boldsymbol{F}_{yi}=F_y(\bar{x}_i,\bar{y}_i,\dot{\bar{x}}_i,\dot{\bar{y}}_i).$$

The Capone correction model[15] is used to simulate oil-film force because it has a simple analytical expression with good accuracy and convergence. The referenced crack model can be seen in Ref. [16].

2.2 Oil film force

In this paper, laminar and isothermal lubrication in short journal bearing assumption is used[15]. According to bearing theory, the dimensionless nonlinear oil-film force can be expressed as

$$\begin{Bmatrix}f_x\\f_y\end{Bmatrix}=-\frac{\sqrt{(x-2y')^2+(y+2x')^2}}{1-x^2-y^2}\bullet \begin{Bmatrix}3xV(x,y,\alpha)-\sin\alpha G(x,y,\alpha)-2\cos\alpha S(x,y,\alpha)\\3yV(x,y,\alpha)+\cos\alpha G(x,y,\alpha)-2\sin\alpha S(x,y,\alpha)\end{Bmatrix}, \tag{3}$$

where x, y are dimensionless displacement in corresponding direction. And

$$V(x,y,\alpha)=\frac{2+(y\cos\alpha-x\sin\alpha)G(x,y,\alpha)}{1-x^2-y^2},$$

$$S(x,y,\alpha)=\frac{x\cos\alpha+y\sin\alpha}{1-(x\cos\alpha+y\sin\alpha)^2},$$

$$\alpha = \arctan\frac{y+2x'}{x-2y'} - \frac{\pi}{2}\operatorname{sgn}\left(\frac{y+2x'}{x-2y'}\right) - \frac{\pi}{2}\operatorname{sgn}(y+2x').$$

The dimensional oil-film force is obtained by $F_x = \sigma P f_x$ and $F_y = \sigma P f_y$. Here, P is half weight of the rotor; μ is the absolute viscosity of lubricant, c is the dimensional thickness of the lubrication film, and σ is the modified Sommerfeld number,

$$\sigma = \frac{m\omega RL}{P}\left(\frac{R}{c}\right)^2\left(\frac{L}{2R}\right)^2.$$

2.3 Dimensionless and reduction of the system equations

Because the system response amplitude is too small, to ensure the precision, the numeric solution usually needs to be nondimensionalized with the following substitutions:

$$\boldsymbol{X} = \frac{\bar{\boldsymbol{X}}}{c},\ \omega t = \tau,\ \dot{\bar{\boldsymbol{X}}} = \frac{\mathrm{d}\bar{\boldsymbol{X}}}{\mathrm{d}\tau}\frac{\mathrm{d}\tau}{\mathrm{d}t} = c\boldsymbol{X}'\omega,$$

$$\ddot{\bar{\boldsymbol{X}}} = \frac{\mathrm{d}\dot{\bar{\boldsymbol{X}}}}{\mathrm{d}\tau}\frac{\mathrm{d}\tau}{\mathrm{d}t} = c\boldsymbol{X}'\omega^2,\ \frac{F_{xi}}{\sigma P} = f_x(x_i, y_i, x_i', y_i'),$$

$$\frac{F_{yi}}{\sigma P} = f_y(x_i, y_i, x_i', y_i').$$

Eq. (1) can be transformed into a convenient dimensionless form:

$$\bar{\boldsymbol{M}}c\Omega^2\boldsymbol{X}'' + \bar{\boldsymbol{C}}c\Omega\boldsymbol{X}' + \bar{\boldsymbol{K}}c\boldsymbol{X} = \boldsymbol{F}(\boldsymbol{X}, \boldsymbol{X}') + \boldsymbol{R}(\tau) + \boldsymbol{G}. \quad (4)$$

If it is assumed that $\boldsymbol{M} = \bar{\boldsymbol{M}}c\Omega^2$, $\boldsymbol{C} = \bar{\boldsymbol{C}}c\Omega$, and $\boldsymbol{K} = \bar{\boldsymbol{K}}c$, and replacing $\boldsymbol{X}'$ and $\boldsymbol{X}''$ by $\dot{\boldsymbol{X}}$ and $\ddot{\boldsymbol{X}}$, Eq. (4) can be written as

$$\boldsymbol{M}\ddot{\boldsymbol{X}} + \boldsymbol{C}\dot{\boldsymbol{X}} + \boldsymbol{K}\boldsymbol{X} = \boldsymbol{F}(\boldsymbol{X}, \dot{\boldsymbol{X}}) + \boldsymbol{R}(\tau) + \boldsymbol{G}. \quad (5)$$

For a finite element system, especially a nonlinear dynamic system, a processing of dimension reduction is needed so as to save computing resources. When the order of the vector components is rearranged in linear and nonlinear parts, to simplify notations, Eq. (5) can be partitioned as

$$\begin{pmatrix}\boldsymbol{M}_{ii} & \boldsymbol{M}_{is}\\ \boldsymbol{M}_{si} & \boldsymbol{M}_{ss}\end{pmatrix}\begin{pmatrix}\ddot{\boldsymbol{X}}_i\\ \ddot{\boldsymbol{X}}_s\end{pmatrix} + \begin{pmatrix}\boldsymbol{C}_{ii} & \boldsymbol{C}_{is}\\ \boldsymbol{C}_{si} & \boldsymbol{C}_{ss}\end{pmatrix}\begin{pmatrix}\dot{\boldsymbol{X}}_i\\ \dot{\boldsymbol{X}}_s\end{pmatrix} +$$
$$\begin{pmatrix}\boldsymbol{K}_{ii} & \boldsymbol{K}_{is}\\ \boldsymbol{K}_{si} & \boldsymbol{K}_{ss}\end{pmatrix}\begin{pmatrix}\boldsymbol{X}_i\\ \boldsymbol{X}_s\end{pmatrix} = \begin{pmatrix}\boldsymbol{0}_i\\ \boldsymbol{F}(\boldsymbol{X}_s, \dot{\boldsymbol{X}}_s)\end{pmatrix} + \begin{pmatrix}\boldsymbol{R}_i(t)\\ \boldsymbol{R}_s(t)\end{pmatrix} + \begin{pmatrix}\boldsymbol{G}_i\\ \boldsymbol{G}_s\end{pmatrix}. \quad (6)$$

As shown in Eq. (6), only components of $X_s \in \mathbf{R}^{N_s}$ are directly subjected to the nonlinear forces, therefore, truncated modal transformation can be used to reduce the DOFs (degrees of freedom) of $X_i \in \mathbf{R}^{N_i}$, ($N_i = N - N_s$), $N = 4n$. We fix the interface freedom X_s in Eq. (6), and structure the fixed interface master mode $\Theta_l = [\psi_l, 0]^{\mathrm{T}}$ with the lower mode ψ_l which is systematic normalized. In addition, given some interface degrees are unit displacements and other interface degrees are zero, the static mode can be derived which is also called "constraint mode". The system constraints modal equation is

$$\boldsymbol{X}_i = -\boldsymbol{K}_{ii}^{-1} \bullet \boldsymbol{K}_{is}\boldsymbol{X}_s. \quad (7)$$

So, the constraints modal set is

$$\Theta_s = \begin{pmatrix}-\boldsymbol{K}_{ii}^{-1}\boldsymbol{K}_{is}\\ \boldsymbol{I}\end{pmatrix}.$$

After assembling the fixed master mode and the constraint mode, the system mode matrix Θ can be written as

$$\Theta = (\Theta_l \quad \Theta_s). \quad (8)$$

Then, the vibration equation in modal coordinates could be written as

$$\hat{\boldsymbol{M}}\ddot{\boldsymbol{U}} + \hat{\boldsymbol{C}}\dot{\boldsymbol{U}} + \hat{\boldsymbol{K}}\boldsymbol{U} = \begin{pmatrix}\boldsymbol{0}_i\\ \boldsymbol{F}(\boldsymbol{X}_s, \dot{\boldsymbol{X}}_s)\end{pmatrix} + \hat{\boldsymbol{R}}(\tau) + \hat{\boldsymbol{G}}, \quad (9)$$

where

$$\hat{\boldsymbol{M}} = \Theta^{\mathrm{T}}\begin{pmatrix}\boldsymbol{M}_{ii} & \boldsymbol{M}_{is}\\ \boldsymbol{M}_{si} & \boldsymbol{M}_{ss}\end{pmatrix}\Theta,\ \hat{\boldsymbol{C}} = \Theta^{\mathrm{T}}\begin{pmatrix}\boldsymbol{C}_{\mathrm{ii}} & \boldsymbol{C}_{\mathrm{is}}\\ \boldsymbol{C}_{\mathrm{si}} & \boldsymbol{C}_{\mathrm{ss}}\end{pmatrix}\Theta,$$

$$\hat{\boldsymbol{K}} = \Theta^{\mathrm{T}}\begin{pmatrix}\boldsymbol{K}_{ii} & \boldsymbol{K}_{is}\\ \boldsymbol{K}_{si} & \boldsymbol{K}_{ss}\end{pmatrix}\Theta,\ \hat{\boldsymbol{R}}(t) = \Theta^{\mathrm{T}}\begin{pmatrix}\boldsymbol{R}_i(t)\\ \boldsymbol{R}_s(t)\end{pmatrix},\ \hat{\boldsymbol{G}} = \Theta^{\mathrm{T}}\begin{pmatrix}\boldsymbol{G}_i\\ \boldsymbol{G}_s\end{pmatrix}.$$

Thus, the number of the equations of the system has been reduced from $N(N_i+N_s)$ to $Q(N_l+N_s)$ where Q is substantially smaller than N. If $\boldsymbol{U}$ is the solution of the equation in mode coordinates, then the vibration response results of the original system can be obtained from the relationship $\boldsymbol{X} = \Theta\boldsymbol{U}$ which can return to the original physical coordinates.

Eqs. (1), (4), (5), and (9) describe a nonlinear dynamic systematic equation in different stage. The approximate solution of these coupled nonlinear differential equations can be obtained by some numerical methods.

Additional, in this paper, the Floquet theory is adopted for distinguishing the periodic instability. And the initial value on the Poincaré section for every rotational speed is seeked by the shooting method which is combined with the Newmark-β. So the accuracy of the initial value can be fully guaranteed.

3 Dynamic Response Analysis

In this section, the impact of the amount of unbalance and the crack depth on the rotor-bearing system with crack is investigated. Fig. 2 displays the instability bifurcation state in the speed-eccentricity domain when the crack depth ratios are d=0.6 and d=0.9, respectively. In Fig. 2, set A (A1, A2) represents the Hopf bifurcation, and set B (B1, B2) represents the period-2 bifurcation. It can be seen from Fig. 2, system instability occurs Hopf bifurcation when crack depth ratio is d=0.6 and disk eccentricity is $b\leqslant$0.065 mm, and instability speed decreases with eccentricity increasing. When $b\geqslant$0.065 mm, system instability shows as period-2 bifurcation, instability speed decreases firstly and then increases with eccentricity going up. Meanwhile, Fig. 2 indicates that when the crack depth ratio is d=0.9, the system bifurcation type is identical with the former, and the instability trends are basically same, but the instability speed of the latter is obviously greater, and the increment is small. According to these phenomena, the presence of cracks does not affect the type of system instability and the instability speed is slightly increasing as the crack depth becomes deeper.

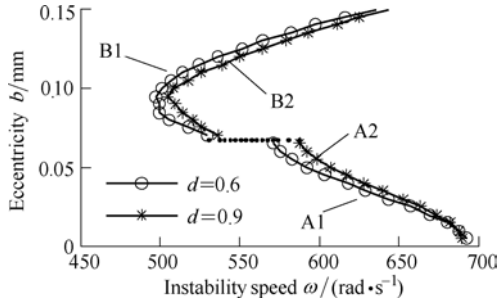

Fig. 2. Bifurcation set of the rotor system with crack in eccentricity-rotational speed parameters plane

In order to verify the validity of the calculation results in Fig. 2, the real and imaginary parts of the maximal Floquet multipliers in some special speeds are listed in Table 2, which demonstrates that the maximal Floquet multiplier run out of the unit circle from negative real axis while the system speed reaches 501 rad/s. It can be determined that a period-2 bifurcation occurs right here. Fig. 3(a) is the diagram of the module of the maximal Floquet multiplier, and Fig. 3(b) describes its changing track in complex field. These diagrams can show the change of the maximal Floquet multiplier in Table 2 more clearly. In order to confirm the validity of the synchronous periodic solution, the system responses are concerned too. The bifurcation diagram of the system is displayed in Fig. 4 which indicates that the system response shows two misaligned points sets beginning at $\omega=501$ rad/s on the Poincaré hyperplane. Thus, the system has a period-2 bifurcation at 501 rad/s, following with the quasi periodic or chaotic motion. This is accord with the previous bifurcation situation. When the system is at $\omega=501$ rad/s and $\omega=520$ rad/s, the oscillogram, axis orbit diogram, Poincaré sectional view and amplitude spectrogram are shown in Fig. 5. From the graph we can see that when the rotational speed is 480 rad/s, the system is stable with a synchronous periodic motion. When the speed is 520 rad/s, the system becomes unstable. The oscillogram shows harmonic wave in Fig. 5(e). The axis orbit figure appears as an inner "8" shape. Two concentration points appear in the Poincaré sectional view. The amplitude spectrogram appears half frequency component and weak double frequency component. But when the speed is 800 rad/s, in Figs. 5(i)–5(l), the oscillogram of system response shows harmonic wave. The axis orbit figure shows a non-repetitive path. Poincaré map shows a closed ring. The amplitude spectrogram of this response shows more combination frequency components of first critical frequency and rotating frequency. These results prove the previous calculation is correct.

Table 2. Maximal Floquet multipliers of synchronous periodic motion when b=0.08 mm

Rotation speed ω/(rad • s^{-1})	Multipliers mold $\lvert\lambda\rvert_{\max}$	Floquet multipliers λ
350	0.296 233	−0.245 726±0.165 447i
400	0.241 984	−0.241 984±0.000 000i
450	0.354 868	−0.347 734±0.070 795i
480	0.829 852	−0.829 852±0.000 000i
490	0.913 487	−0.913 487±0.000 000i
500	0. 995 491	−0.995 491±0.000 000i
501	**1.002 527**	**−1.002 527±0.000 000i**
502	1.000 902	−1.000 902±0.000 000i
505	1.033 440	−1.033 440±0.000 000i
510	1.069 406	−1.069 406±0.000 000i

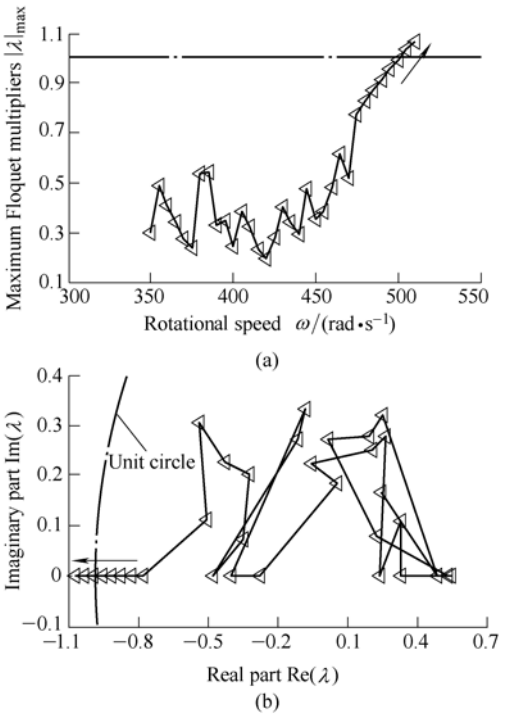

Fig. 3. Diagrams of the Floquet multipliers for synchronous periodic motion when b=0.08 mm

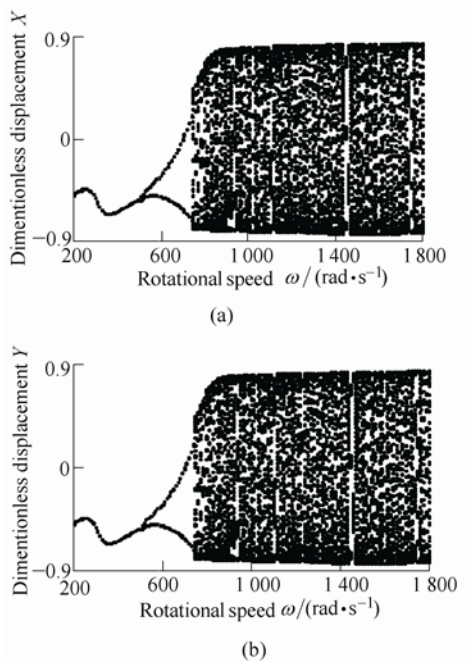

Fig. 4. Bifurcation diagrams at the right bearing when b=0.05 mm

The previous response process of the system with unbalance parameter b=0.08 mm shows period- doubling bifurcation instability. In this section, we change the parameter b=0.05 mm, and still keep the crack depth d=0.6. Under this working condition, the real and imaginary parts of the maximal Floquet multipliers in some special speeds are listed in Table 3 which shows that the maximal Floquet multiplier run out of the unit circle from negative real axis while the system speed reaches 592 rad/s. From this, we can conclude that a Hopf bifurcation occurs right here.

Similarly, Fig. 6 is the diagram of the maximal Floquet multiplier which can display the change of the maximal Floquet multiplier in Table 3 more clearly. In order to confirm the validity of the prediction conclusion by shooting method in Table 3 and Fig. 6, the system response is studied. The bifurcation diagram of the system is displayed Fig. 7. The system response shows a series of misaligned point sets beginning at $\omega = 592$ rad/s on the Poincaré hyperplane which is the same as that in the Table 3 and Fig. 6, the system has a Hopf bifurcation at 592 rad/s, and then a small length of period-doubling motion happens. This is consistent with the preceding result. When the system is at $\omega = 550$ rad/s, $\omega = 600$ rad/s, $\omega = 700$ rad/s and $\omega = 800$ rad/s, the oscillogram, axis orbit diagram, Poincaré sectional view and amplitude spectrogram are shown in Fig. 8. It can be seen from the graphs that when the rotational speed is 550 rad/s, the system is stable with a synchronous periodic motion; while when the speed is 600 rad/s, the system becomes unstable. The oscillogram shows harmonic wave in Fig. 8(e). The axis orbit figure

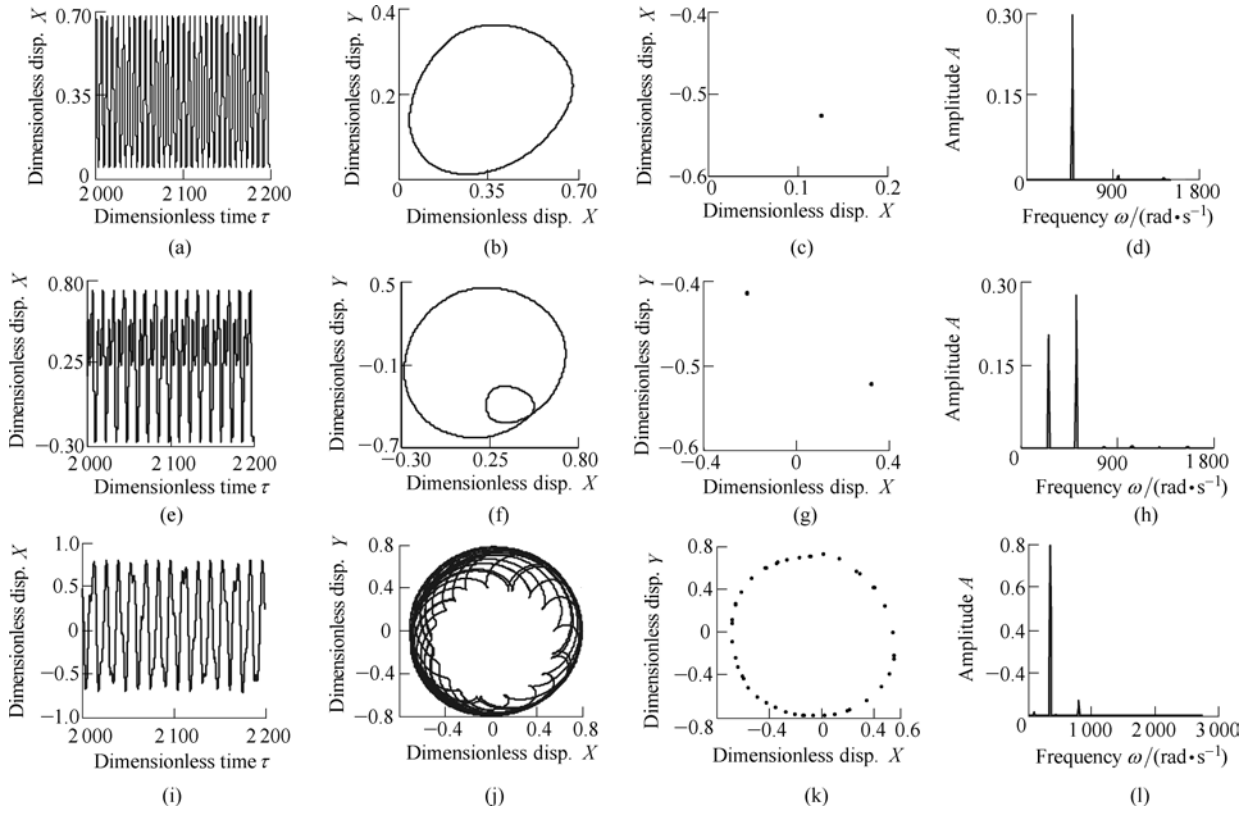

Fig. 5. Time wave plots, trajectories, Poincaré maps and amplitude spectra when b=0.08mm

appears as a non-repetitive path. A closed ring is made up by some concentration points in the Poincaré sectional view. Rotating frequency component and half frequency component appear in amplitude spectrogram. When the speed is 700 rad/s, in Figs. 8(i)–8(l), the oscillogram of system response shows week harmonic wave; the axis orbit figure displays a repeating ring, but the Poincaré sectional view is two misaligned points; the amplitude spectrogram of this response shows a strong half frequency component and a weekly rotating frequency component. These results mean that the shaft rotates in a half-speed whirl motion at 700 rad/s. When the speed is 800 rad/s, the oscillogram of system response shows week harmonic wave too; the axis orbit figure is a non-repetitive path but the Poincaré sectional view displays a closed ring; the amplitude spectrogram of this response shows a strong first critical frequency component, a week rotating frequency component and some other frequency components which cannot be common divisor. It can be concluded that the shaft rotated in a quasi-period motion. All these results also prove the previous calculation is correct.

From above results the following conclusions can be conducted. The accurate calculation results are obtained by the prediction method in this paper. The depth of the crack influence on the system instability speed and the bifurcation form slightly. A deeper crack can lead to a larger instability speed of the rotor system, but the change is small. On the contrary, for the same crack fault, the unbalance has a more remarkable impact on the instability speed and the bifurcation form of the system.

Table 3. Floquet multipliers of synchronous periodic motion when b=0.05 mm

Rotation speed ω/(rad • s^{-1})	Multipliers mold $\lvert\lambda\rvert_{\max}$	Floquet multipliers λ
350	0.283 208	−0.096 309±0.266 330i
450	0.685 437	−0.651 638±0.212 584i
550	0.932 609	−0.930 423±0.063 815i
580	0.985 719	−0.973 533±0.154 519i
591	0.999 394	−0.982 090±0.185 170i
592	**1.000 902**	**−0.983 050±0.188 193i**
593	1.002 404	−0.983 997±0.191 219i
595	1.005 457	−0.985 906±0.197 312i

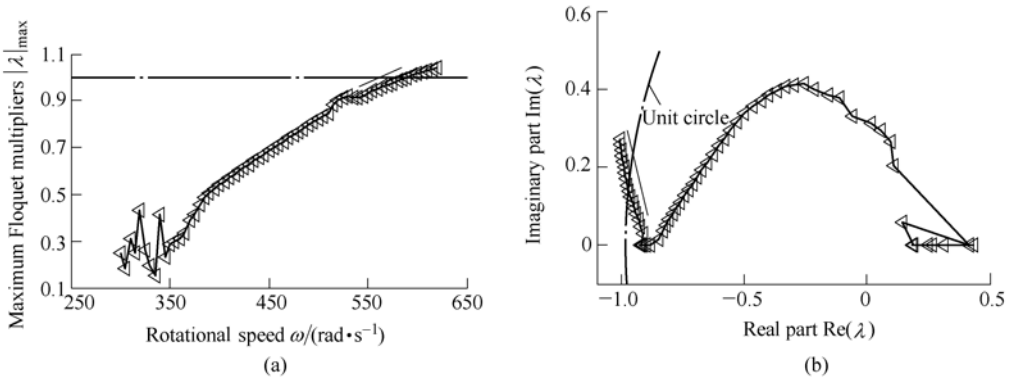

Fig. 6. Curve of the Floquet multipliers for synchronous periodic motion when b=0.05 mm

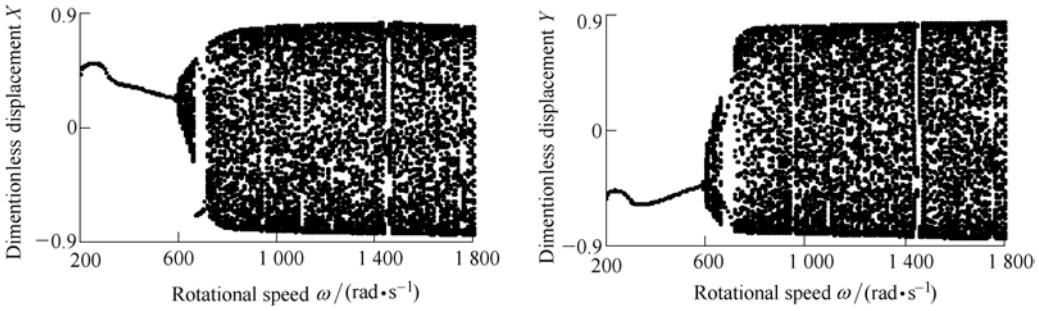

Fig. 7. Bifurcation diagrams at the right bearing when b=0.05 mm

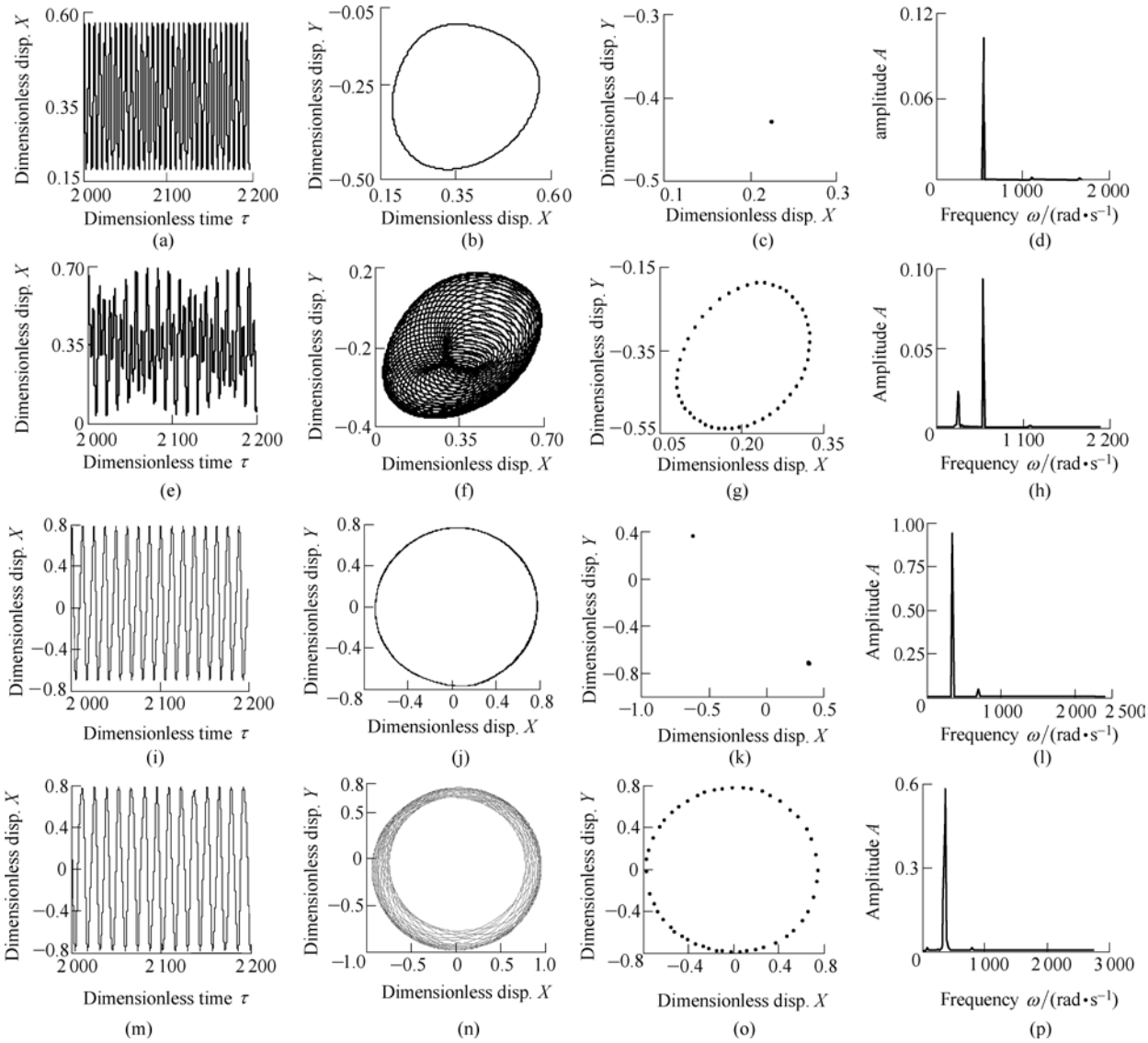

Fig. 8. Time wave plot, trajectory, Poincaré maps and amplitude spectra when b=0.05mm

4 Experiment and Analysis

An experiment rig is built based on the dynamic similarity principle, as is shown in

Fig. 9. Here a shaft with crack depth ratio d=0.6 is used in order to investigate the effects of eccentricity on system motion stability.

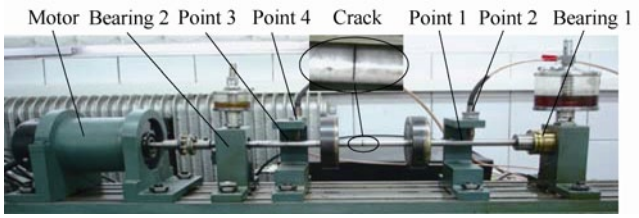

Fig. 9. Experimental rig of rotor-bearing system

Fig. 10 is the three-dimensional spectrum of measuring point 1, where f_n is the first-order critical speed of the system, 1X and 2X line represent rotational frequency and double frequency spectrum amplitude, respectively. As is shown in the Fig. 10, oil-whirl appears at time t_1, and disappears at t_2, then "locking frequency" appears, until time t_3, the vibration during this time is oil whip firstly, and then oil-whirl appeared at t_3, then disappears at t_4. Furthermore, double rotational frequency appears in amplitude spectrum due to the existence of crack fault. The responses after system becomes instable are shown in Fig. 11 and Fig. 12, respectively. Fig. 9 shows the response of measuring point 1 when ω=636 rad/s, trajectory of measuring point 1 indicates the quasi-periodic motion at this moment, and a half rotational frequency 1/2X can be seen in amplitude spectra, so it is considered that the system is undergoing a quasi-periodic instability at this time. Fig. 12 displays the response of measuring point 1 when ω=1 043 rad/s. It can be seen that system is in a state of instability, amplitude spectra shows oil whip appears at this moment, and dominant amplitude in frequency spectrum is greater than amplitude of rotational frequency at first-order critical speed. In addition, the

combination frequencies also appear at the same time such as f_2=1X+f_n and f_3=1X+f_1. Besides, double rotational frequency component also appears because of crack fault.

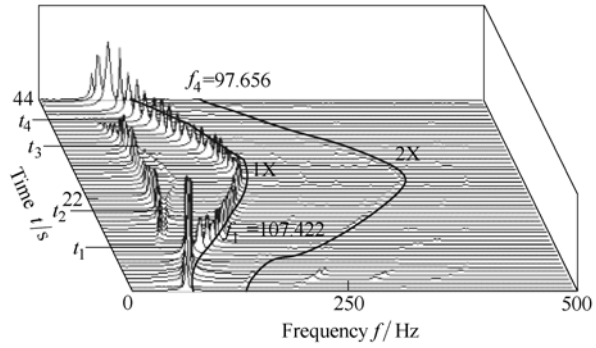

Fig. 10. The global three-dimensional spectrogram of the rotor-bearing system with small eccentricity

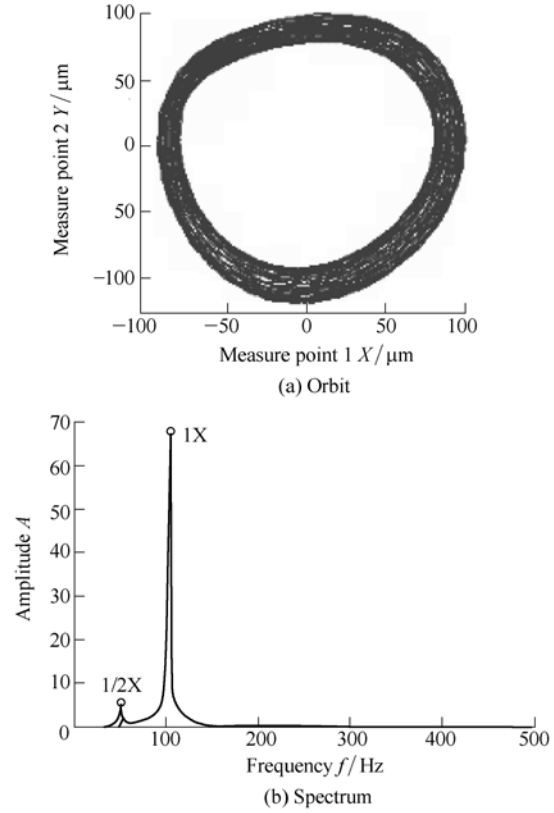

Fig. 11. Response of the rotor-bearing system at ω=636 rad/s

Fig. 13 gives the three-dimensional spectrum of measuring point 1 when the eccentricity of the disks becomes larger while the other experiment conditions keeps same (crack depth ratio d=0.6). f_n, 1X and 2X line are also given in the figure. Oil whirl appears at t_1 until t_2 when oil whip appears and this lasts until t_3. At the same time oil whirl appeared again and it disappeared at t_4. It should be noted that when rotation frequency is f_1=91.797 Hz at t_1 and f_4=85.938 Hz at t_4, an obvious "lagging" phenomenon can be found. It can be concluded that the instability speed decreases due to the increase of eccentricity which is consistent with the previous calculation. Furthermore, two times rotational frequency appears in the frequency spectrum because of the crack fault, but not obviously.

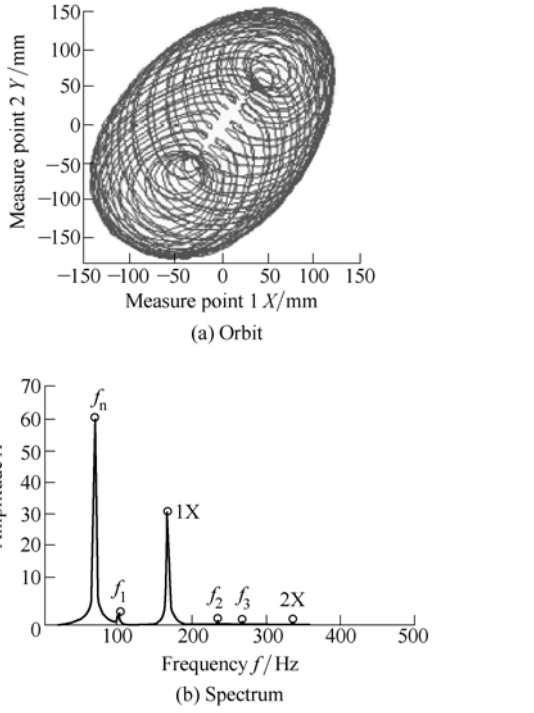

Fig. 12. Response of the rotor-bearing system at ω=1043 rad/s

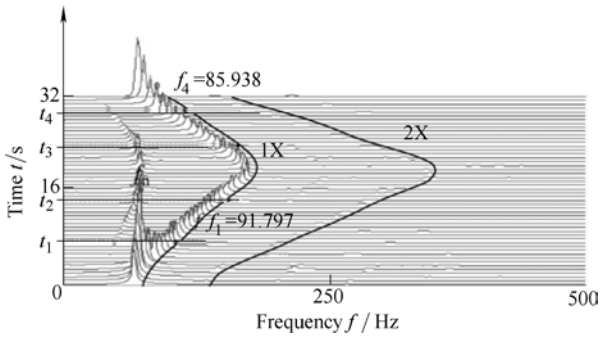

Fig. 13. Global three-dimensional spectrogram of the rotor system with greater eccentricity

The responses after system becomes instable are shown in Fig. 14 and Fig. 15 respectively. The former gives the response of measuring point 1 when ω=611 rad/s. The quasi-periodic motion can be indicated easily in the trajectory of measuring point 1 at this moment, 1/2 times and 2 times rotational speed amplitude can be seen in amplitude spectra. The latter gives the response of measuring point 1 when ω=835 rad/s. Amplitude spectra shows oil whip appeared at this moment, and combination frequencies appears, for example, f_1=1X+f_n. Besides, double rotational frequency component also appears due to the crack fault.

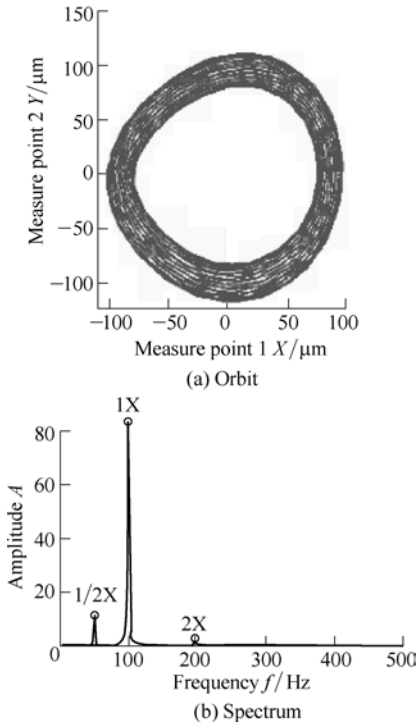

Fig. 14. Response of the rotor-bearing system at ω=611 rad/s

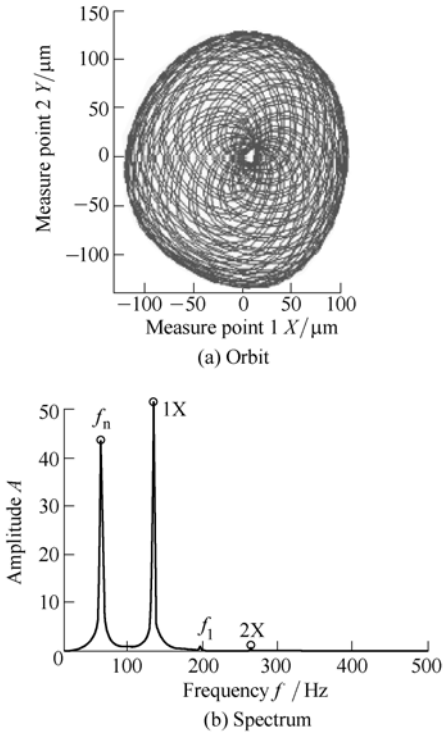

Fig. 15. Response of the rotor-bearing system at ω=835 rad/s

It comes to a conclusion from previous experiment that increasing eccentricity will reduce the instability speed slightly for the system with crack depth ratio d=0.6, and "lag phenomenon" and the frequency combination phenomenon occurs together.

5 Conclusions

(1) Because of the disturbance to formation of the oil whirl by crack fault, the instability speed increases slightly as the crack becomes deeper. But this does not mean that the existence of cracks should be ignored. The crack deep enough will cause the shaft breakage. Furthermore, the effect of eccentricity on system stability is greater than that caused by crack fault by contrast.

(2) With the influence of system eccentricity, the instability speed does not show the monotonically trend, but decreases firstly and then increases, and as the type of instability changes, the instability speed jumps concomitantly.

(3) Cooperation between shooting method and the Newmark-β is an effective strategy to study the period instability on the rotor-bearing system, the numerical method and the Floquet theory can be adopted for the reduced FE system.

References

[1] GASCH R. A survey of the dynamic behavior of a simple rotating shaft with a transverse crack[J]. *Journal of Sound and Vibration*, 1993, 160(2): 313–332.

[2] LEE C W. Modeling of a simple rotor with a switching crack and its experimental verification[J]. *ASME Journal of Vibration and Acoustics*, 1992, 114(2): 217–225.

[3] CHAN R K, LAI T C. Digital simulation of a rotating shaft with a transverse crack[J]. *Applied Mathematical Modeling*, 1995, 19(7), 411–420.

[4] MENG G, GASCH R. Stability and stability degree of a cracked flexible rotor supported on journal bearings[J]. *ASME Journal of Vibration and Acoustics*, 2000, 122(2): 116–125.

[5] WAN Fangyi, XU Q, LI S, Vibration analysis of cracked rotor sliding bearing system with rotor-stator rubbing by harmonic wavelet transform[J]. *Journal of Sound and Vibration*, 2004, 271(3–5): 507–518.

[6] ZHENG Jibing, MENG Guang. Analysis of the stability of a cracked rotor supported on journal bearings via chebyshev polynomials[J]. *Journal of Northwestern Polytechnical University*, 1997, 15(3): 383–388.

[7] PATEL T H, DARPE A K. Vibration response of a cracked rotor in presence of rotor-stator rub[J]. *Journal of Sound and Vibration*, 2008, 317(3–5): 841–865.

[8] PATEL T H, DARPE A K. Study of coast-up vibration response for rub detection[J]. *Mechanism and Machine Theory*, 2009, 44(8): 1 570–1 579.

[9] LIU Changli, ZHENG Jianrong, ZHOU Wei. On the bifurcation and stability of periodic motion of rotor-bearing systems with crack and pedestal looseness fault[J]. *Journal of Vibration and Shock*, 2007, 26(11): 13–17.

[10] LUO Yuegang, ZHANG Songhe, LIU Xiaodong. Stability of a two-span rotor- bearing system with crack fault[J]. *Transactions of the Chinese Society for Agricultural Machinery*, 2007, 38(5): 168–172.

[11] ZHENG T, HASEBE N. An efficient analysis of high-order dynamical system with local nonlinearity[J]. *Journal of Vibration and Acoustics*, 1999, 121(3): 408–416.

[12] ZHENG T, HASEBE N. Nonlinear dynamic behaviors of a complex rotor-bearing system[J]. *Journal of Applied Mechanics*, 2000, 67(3): 485–495.

[13] JING Jianping, MENG Guang, SUN Yi, et al. On the non-linear dynamic behavior of a rotor-bearing system[J]. *Journal of Sound and Vibration*, 2004 274(3–5): 1 031–1 044.
[14] JING Jianping, MENG G,uang SUN Yi, et al. On the oil-whipping of a rotor-bearing system by a continuum model[J]. *Applied Mathematical Modelling*, 2005, 29(5): 461–475.
[15] ADILETTA G, GUIDO A R, ROSSI C. Chaotic motions of a rigid rotor in short journal bearings[J]. *Nonlinear Dynamics*, 1996, 10(3) 251–269.
[16] MAYES I W. Analysis of the response of a multi-rotor-bearing system containing a transverse crack in a rotor[J]. *ASME Journal of Vibration, Acoustics, Stress, and Reliability in Design*, 1984, 106(2): 139–145.
[17] LI Chaofeng, LI He, MA Hui. Bifurcation and stability of the flexible rotor-bearing system with rub-impact by a continuum model[J]. *Journal of Mechanical Engineering*, 2010, 46(11), 107–113. (in Chinese)

Biographical notes

LI Chaofeng, born in 1980, is currently a lecturer at *School of Mechanical Engineering & Automation, Northeastern University, China*. He received his PhD degree from *Northeastern University, China*, in 2010. His main research interests include rotor *dynamics, mechanical vibration and contro*l and *dynamic design of mechanical products.*
Tel: +86-24-83684491; E-mail: chfli@mail.neu.edu.cn

YU Hexing, born in 1989, is currently a master candidate at *School of Mechanical Engineering & Automation, Northeastern University, China*.
E-mail: yhx.neu@gmail.com

ZHOU Shihua, born in 1987, is currently a master candidate at *School of Mechanical Engineering & Automation, Northeastern University, China*.
E-mail: zhou_shihua@126.com

WEN Bangchun, born in 1930, is currently a professor at *School of Mechanical Engineering & Automation, Northeastern University, China*. His main research interests include vibration utilization engineering, rotor dynamics, nonlinear vibration and applications of mechanical engineering, vibration diagnostics of the machine fault, mechanical-electronic integration and the machinery engineering theories.
E-mail: bcwen1930@sina.com.cn